

Microscopic self-energy calculations and dispersive optical-model potentialsS. J. Waldecker,¹ C. Barbieri,^{2,3,*} and W. H. Dickhoff¹¹*Department of Physics, Washington University, St. Louis, Missouri 63130, USA*²*Department of Physics, Faculty of Engineering and Physical Sciences, University of Surrey, Guildford, Surrey GU2 7XH, United Kingdom*³*Theoretical Nuclear Physics Laboratory, RIKEN Nishina Center, 2-1 Hirosawa, Wako, Saitama 351-0198, Japan*

(Received 21 May 2011; revised manuscript received 11 August 2011; published 29 September 2011)

Nucleon self-energies for $^{40,48,60}\text{Ca}$ isotopes are generated with the microscopic Faddeev-random-phase approximation (FRPA). These self-energies are compared with potentials from the dispersive optical model (DOM) that were obtained from fitting elastic-scattering and bound-state data for $^{40,48}\text{Ca}$. The *ab initio* FRPA is capable of explaining many features of the empirical DOM potentials including their nucleon asymmetry dependence. The comparison furthermore provides several suggestions to improve the functional form of the DOM potentials, including among others the exploration of parity and angular momentum dependence. The nonlocality of the FRPA imaginary self-energy, illustrated by a substantial orbital angular momentum dependence, suggests that future DOM fits should consider this feature explicitly. The roles of the nucleon-nucleon tensor force and charge-exchange component in generating the asymmetry dependence of the FRPA self-energies are explored. The global features of the FRPA self-energies are not strongly dependent on the choice of realistic nucleon-nucleon interactions.

DOI: [10.1103/PhysRevC.84.034616](https://doi.org/10.1103/PhysRevC.84.034616)

PACS number(s): 21.10.Pc, 24.10.Ht

I. INTRODUCTION

The properties of nucleons propagating in the nucleus exhibit characteristic deviations from the naive shell-model picture. At positive energies, corresponding to the domain of elastic scattering, there is unambiguous evidence that the potential (or self-energy) that a nucleon experiences is absorptive [1–3]. This simple observation has important implications, since it shows that nuclear states cannot be interpreted only in terms of a simple shell-model potential that is real and independent of energy. The importance of the dynamic aspects of the nuclear shell model was recognized in Ref. [4]. The link between optical potentials and the traditional bound-state shell model was explored by Mahaux and Sartor [5] and extensively reviewed in Ref. [6]. These authors realized that information on nucleon propagation at positive energy influences the properties of the real nuclear potential at negative energy, since the nucleon self-energy obeys a dispersion relation that links the real part to its imaginary part at all energies (see, e.g., Ref. [7]). Mahaux and Sartor exploited standard representations of the imaginary part of the optical potential in terms of volume and surface contributions. They further assumed that the behavior of the imaginary potential was similar near both sides of the Fermi energy and used a subtracted form of the dispersion relation to obtain the corresponding real part. By performing this subtraction at the Fermi energy, only the additional knowledge of the real potential at that energy is required. The resulting optical potential is now called the dispersive optical model (DOM).

Recent applications of the DOM have concentrated on the nucleon asymmetry dependence by simultaneously fitting data pertaining to different calcium isotopes [8,9] and to

spherical isotopes up to tin and ^{208}Pb [10]. Such an analysis can be utilized to predict properties of isotopes with larger nucleon asymmetry by extrapolating the DOM potentials. Such data-driven extrapolations present a reliable strategy to approach and predict properties of isotopes toward the respective drip lines, since they can be tested by performing appropriate experiments. An important feature extracted from this analysis is the increase in surface absorption of protons in heavier Ca isotopes for increasing asymmetry. While this trend is unambiguous, there is no clear understanding of the underlying dynamics responsible for it. A much weaker and opposite trend was inferred for neutrons. It is therefore useful to study the nucleon self-energy—which is the microscopic counterpart of the DOM—to clarify this behavior and provide a deeper understanding of the DOM potentials.

Microscopic approaches to optical potentials include, e.g., the Feshbach formalism [11,12], the many-body Green's function theory [13], and the G -matrix folding approximation [14]. Both the Feshbach and Green's function approaches are exact microscopic theories for the optical potential and are closely related. Feshbach originally developed his formalism by projecting the many-body Hamiltonian on the subspace of scattering states, in which the scattered nucleon is added on top of the target wave function. This subspace includes all the single-nucleon scattering and $(A + 1)$ -nucleon bound states. However, it cannot describe the so-called Pauli-blocked (or hole) states that correspond to occupied orbits below the Fermi surface and can be reached only through nucleon removal processes. It has been proven that if Feshbach's theory is extended to a space including states both above and below the Fermi surface, the resulting optical potential corresponds exactly to the irreducible self-energy $\Sigma^*(E)$ [13] (see also Refs. [15,16] for a shorter demonstration). The Green's function method is ideally suited to pursue a microscopic understanding of the nucleon self-energy at both positive and negative energies [17]. Both the propagator

*Permanent address: University of Surrey, Guildford, UK; c.barbieri@surrey.ac.uk

and the self-energy $\Sigma^*(E)$ of the Green's function method can be cast in the form of dispersion relations which are merely a consequence of their analytic properties [see Eqs. (1) and (4) below] associated with the correct time ordering for adding and removing a nucleon. Hence, the dispersion relations represent a constraint imposed by causality. The above equivalence with the microscopic optical potential is fundamental for the present study, since the available knowledge from calculations based on the Green's function theory can be employed to suggest improvements of optical models. In particular, in the DOM the dispersion relation obeyed by $\Sigma^*(E)$ is used to reduce the number of parameters and to enforce the effects of causality. Thus, the DOM potentials can also be thought of as a representation of the nucleon self-energy.

The most sophisticated microscopic implementation of the Green's function method considers the role of long-range or low-energy correlations in which nucleons couple to low-lying collective states and giant resonances. This is accomplished by using the random phase approximation (RPA) to calculate phonons of particle-particle (hole-hole) and particle-hole types. These are then summed to all orders in a Faddeev summation for both two-particle-one-hole (2p1h) and two-hole-one-particle (2h1p) propagation. This approach is referred to as Faddeev random phase approximation (FRPA) [18,19]. This method is size extensive and has been successfully benchmarked for soft interactions in purely *ab initio* calculations for ${}^4\text{He}$ [20], giving results of comparable accuracy to coupled-cluster theory.

The FRPA was originally developed to describe the self-energy of the double closed-shell nucleus ${}^{16}\text{O}$ [19,21]. Subsequently, the method has been applied to atoms and molecules [18,22] and recently to ${}^{56}\text{Ni}$ [23] and ${}^{48}\text{Ca}$ [24]. The *ab initio* results of Ref. [24] are in good agreement with (*e*, *e'* *p*) data for spectroscopic factors from Ref. [25] and also show that the configuration space needed for the incorporation of long-range (surface) correlations is much larger than the space that can be utilized in large-scale shell-model diagonalizations. In Ref. [26], the FRPA was employed to calculate proton scattering on ${}^{16}\text{O}$ and obtain results for phase shifts and low-lying states in ${}^{17}\text{F}$. However, the properties of the self-energy at larger scattering energies which are now of great interest for the developments of DOM potentials were not addressed. In particular, one may expect to extract useful information regarding the functional form of the DOM from a study of the self-energy for a sequence of calcium isotopes. It is the purpose of the present work to close this gap. We have chosen in addition to ${}^{40}\text{Ca}$ and ${}^{48}\text{Ca}$ also to include ${}^{60}\text{Ca}$, since the latter isotope was studied with a DOM extrapolation in Refs. [8,9]. Some preliminary results of these FRPA calculations for spectroscopic factors were reported in Ref. [20], but the emphasis in the present work is on the properties of the microscopically calculated self-energies. The resulting analysis is intended to provide a microscopic underpinning of the qualitative features of empirical optical potentials. Additional information concerning the degree and form of the nonlocality of both the real and imaginary parts of the self-energy will also be addressed because it is of importance

to assess the current local implementations of the DOM method.

In Sec. II A we introduce some of the basic properties for the analysis of the self-energy. The ingredients of the FRPA calculation are presented in Sec. II C. The choice of model space and realistic nucleon-nucleon (NN) interaction are discussed in Sec. III. We present our results in Sec. IV and finally draw conclusions in Sec. V.

II. FORMALISM

In the Lehmann representation, the one-body Green's function is given by

$$g_{\alpha\beta}(E) = \sum_n \frac{\langle \Psi_0^A | c_\alpha | \Psi_n^{A+1} \rangle \langle \Psi_n^{A+1} | c_\beta^\dagger | \Psi_0^A \rangle}{E - (E_n^{A+1} - E_0^A) + i\eta} + \sum_k \frac{\langle \Psi_0^A | c_\beta^\dagger | \Psi_k^{A-1} \rangle \langle \Psi_k^{A-1} | c_\alpha | \Psi_0^A \rangle}{E - (E_0^A - E_k^{A-1}) - i\eta}, \quad (1)$$

where α, β, \dots , label a complete orthonormal basis set, and c_α (c_β^\dagger) are the corresponding second quantization destruction (creation) operators. In these definitions, $|\Psi_n^{A+1}\rangle$, $|\Psi_k^{A-1}\rangle$ are the eigenstates, and E_n^{A+1} , E_k^{A-1} the eigenenergies of the $(A \pm 1)$ -nucleon isotope. The structure of Eq. (1) is particularly useful for our purposes. At positive energies, the residues of the first term, $\langle \Psi_n^{A+1} | c_\alpha^\dagger | \Psi_0^A \rangle$, contain the scattering wave functions for the elastic collision of a nucleon off the $|\Psi_0^A\rangle$ ground state, while at negative energies they give information on final states of the nucleon capture process. Consequently, the second term has poles below the Fermi energy E_F which carry information about the removal of a nucleon and therefore clarify the structure of the target state $|\Psi_0^A\rangle$ itself. Green's function theory provides a natural framework for describing physics both above and below the Fermi surface in a consistent manner.

The propagator (1) can be obtained as a solution of the Dyson equation,

$$g_{\alpha\beta}(E) = g_{\alpha\beta}^{(0)}(E) + \sum_{\gamma\delta} g_{\alpha\gamma}^{(0)}(E) \Sigma_{\gamma\delta}^*(E) g_{\delta\beta}(E), \quad (2)$$

in which $g^{(0)}(E)$ is the propagator for a free nucleon (moving only with its kinetic energy). $\Sigma^*(E)$ is the irreducible self-energy and represents the interaction of the projectile (ejectile) with the target nucleus.

A. Self-energy

For a $J = 0$ nucleus, all partial waves (ℓ, j, τ) are decoupled, where ℓ, j label the orbital and total angular momentum and τ represents its isospin projection. The irreducible self-energy in coordinate space (for either a proton or a neutron) can be written in terms of the harmonic-oscillator basis used

in the FRPA calculation as follows:

$$\begin{aligned} \Sigma^*(\mathbf{x}, \mathbf{x}'; E) &= \sum_{\ell j m_j \tau} \mathcal{I}_{\ell j m_j}(\Omega, \sigma) \\ &\times \left[\sum_{n_a, n_b} R_{n_a \ell}(r) \Sigma_{ab}^*(E) R_{n_b \ell}(r') \right] [\mathcal{I}_{\ell j m_j}(\Omega', \sigma')]^*, \end{aligned} \quad (3)$$

where $\mathbf{x} \equiv \mathbf{r}, \sigma, \tau$. The spin variable is represented by σ , n is the principal quantum number of the harmonic oscillator, and $a \equiv (n_a, \ell, j, \tau)$ (note that for a $J = 0$ nucleus the self-energy is independent of m_j). The standard radial harmonic-oscillator function is denoted by $R_{n\ell}(r)$, while $\mathcal{I}_{\ell j m_j}(\Omega, \sigma)$ represents the j -coupled angular-spin function.

We directly calculate the harmonic-oscillator projection of the self-energy, which can be written as

$$\begin{aligned} \Sigma_{ab}^*(E) &= \Sigma_{ab}^\infty(E) + \tilde{\Sigma}_{ab}(E) \\ &= \Sigma_{ab}^\infty(E) + \sum_r \frac{m_a^r (m_b^r)^*}{E - \varepsilon_r \pm i\eta}. \end{aligned} \quad (4)$$

The term with the tilde is the dynamic part of the self-energy due to long-range correlations calculated in the FRPA, and $\Sigma_{ab}^\infty(E)$ is the correlated Hartree-Fock term which acquires an energy dependence through the energy dependence of the G -matrix effective interaction (see below). $\Sigma_{ab}^\infty(E)$ is the sum of the strictly correlated Hartree-Fock diagram (which is energy independent) and the dynamical contributions due to short-range interactions outside the chosen model space. The self-energy can be further decomposed in a central (0) part and a spin-orbit (ℓs) part according to

$$\Sigma^{\ell j >} = \Sigma_0^\ell + \frac{\ell}{2} \Sigma_{\ell s}^\ell, \quad (5a)$$

$$\Sigma^{\ell j <} = \Sigma_0^\ell - \frac{\ell + 1}{2} \Sigma_{\ell s}^\ell, \quad (5b)$$

with $j_{>,<} \equiv \ell \pm \frac{1}{2}$. The corresponding static terms are denoted by $\Sigma_0^{\infty,\ell}$ and $\Sigma_{\ell s}^{\infty,\ell}$, and the corresponding dynamic terms are denoted by $\tilde{\Sigma}_0^\ell$ and $\tilde{\Sigma}_{\ell s}^\ell$.

The FRPA calculation employs a discrete single-particle basis in a large model space which results in a substantial number of poles in the self-energy (4). Since the goal is to compare the self-energy with optical potentials at positive energy, it is appropriate to smooth out these contributions by employing a finite width for these poles. We note that the optical potential was always intended to represent an average smooth behavior of the nucleon self-energy [6]. In addition, it makes physical sense to at least partly represent the escape width of the continuum states by this procedure. Finally, further spreading of the intermediate states to more complicated states (3p2h and higher excitations that are not included in the present calculation) can also be accounted for by this procedure. Thus, before comparing the self-energy to the DOM potentials, the dynamic part of the microscopic self-energy was smoothed out using a finite, energy-dependent

width for the poles:

$$\tilde{\Sigma}_{n_a, n_b}^{\ell j}(E) = \sum_r \frac{m_{n_a}^r m_{n_b}^r}{E - \varepsilon_r \pm i\eta} \longrightarrow \sum_r \frac{m_{n_a}^r m_{n_b}^r}{E - \varepsilon_r \pm i\Gamma(\varepsilon_r)}. \quad (6)$$

Solving for the real and imaginary parts we obtain

$$\begin{aligned} \tilde{\Sigma}_{n_a, n_b}^{\ell j}(E) &= \sum_r \frac{(E - \varepsilon_r)}{(E - \varepsilon_r)^2 + [\Gamma(\varepsilon_r)]^2} m_{n_a}^r m_{n_b}^r \\ &+ i \left[\theta(E_F - E) \sum_h \frac{\Gamma(\varepsilon_h)}{(E - \varepsilon_h)^2 + \Gamma(\varepsilon_h)^2} m_{n_a}^h m_{n_b}^h \right. \\ &\left. - \theta(E - E_F) \sum_p \frac{\Gamma(\varepsilon_p)}{(E - \varepsilon_p)^2 + [\Gamma(\varepsilon_p)]^2} m_{n_a}^p m_{n_b}^p \right], \end{aligned} \quad (7)$$

where r implies a sum over both particle and hole states, h denotes a sum over the hole states only, and p denotes a sum over the particle states only. For the width, the following form was used [27]:

$$\Gamma(E) = \frac{1}{\pi} \frac{a(E - E_F)^2}{(E - E_F)^2 - b^2}$$

with $a = 12$ MeV and $b = 22.36$ MeV. This generates a narrow width near E_F that increases as the energy moves away from the Fermi surface, in accordance with observations.

In the DOM representation of the optical potential the self-energy is recast in the form of a subtracted dispersion relation

$$\Sigma_{ab}^*(E) = \Sigma_{ab, S}^\infty + \tilde{\Sigma}_{ab}(E)_S, \quad (8)$$

where¹

$$\Sigma_{ab, S}^\infty = \Sigma_{ab}^*(E_F), \quad (9)$$

$$\tilde{\Sigma}_{ab}(E)_S = \Sigma_{ab}^*(E) - \Sigma_{ab}^*(E_F). \quad (10)$$

For the imaginary potential, this is the same as the above defined self-energies (4), and it can therefore be directly compared to the DOM potential. For the real parts we will employ either the normal or the subtracted form in the following as appropriate.

B. Volume integrals

In fitting optical potentials, it is usually found that volume integrals are well constrained by the experimental data [6,28]. For this reason, they have been considered as a reliable measure of the total strength of a potential. For a nonlocal and ℓ -dependent potential of the form (3) it is convenient to consider separate integrals for each angular momentum component, $\Sigma_0^\ell(r, r')$ and $\Sigma_{\ell s}^\ell(r, r')$, which correspond to the square brackets in Eq. (3) and decomposed according to (5). Labeling the central real part of the optical potential with V ,

¹It is the (real) $\Sigma_{ab, S}^\infty$ and the imaginary part of $\tilde{\Sigma}_{ab}(E)_S$ that are parametrized in the DOM potential. $\text{Re } \tilde{\Sigma}_{ab}(E)_S$ is then fixed by the subtracted dispersion relation.

and the central imaginary part by W , we calculate

$$J_W^\ell(E) = 4\pi \int dr r^2 \int dr' r'^2 \text{Im} \Sigma_0^\ell(r, r'; E), \quad (11a)$$

$$J_V^\ell(E) = 4\pi \int dr r^2 \int dr' r'^2 \text{Re} \Sigma_0^\ell(r, r'; E). \quad (11b)$$

We also employ the volume integral of the central real part at the Fermi energy denoted by $J_F^\ell = J_V^\ell(E_F)$, and the corresponding averaged quantities

$$J_W^{\text{avg}}(E) = \frac{1}{N_{\{\ell\}}} \sum_{\ell \in \{\ell\}} J_W^\ell(E), \quad (12a)$$

$$J_V^{\text{avg}}(E) = \frac{1}{N_{\{\ell\}}} \sum_{\ell \in \{\ell\}} J_V^\ell(E). \quad (12b)$$

In Eqs. (12a) and (12b) $N_{\{\ell\}}$ is the number of partial waves included in the average, and the sum runs over all values of ℓ except if otherwise indicated. We also introduce the notation $J_F^{\text{avg}} = J_V^{\text{avg}}(E_F)$.

The correspondence between the above definitions and the volume integrals used for the (local) DOM potential in Refs. [8,9] can be obtained by casting a spherical local potential $U(r)$ into a nonlocal form $U(\mathbf{r}, \mathbf{r}') = U(r)\delta(\mathbf{r} - \mathbf{r}')$. Expanding this in spherical harmonics gives

$$U(\mathbf{r}, \mathbf{r}') = \sum_{\ell m} U^\ell(r, r') Y_{\ell m}^*(\Omega') Y_{\ell m}(\Omega), \quad (13)$$

with the ℓ projection

$$U^\ell(r, r') = \frac{U(r)}{r^2} \delta(r - r'), \quad (14)$$

which is actually angular-momentum independent. The definition (11) for the volume integrals leads to

$$\begin{aligned} J_U^\ell &= 4\pi \int dr r^2 \int dr' r'^2 U^\ell(r, r') \\ &= 4\pi \int U(r) r^2 dr = \int U(r) dr, \quad \text{for any } \ell \end{aligned} \quad (15)$$

and reduces to the usual definition of the volume integral for local potentials. Thus, Eqs. (11) and (12) can be directly compared to the corresponding integrals determined in previous studies of the DOM.

C. Ingredients of the Faddeev-random-phase approximation

The self-energy is shown in terms of Feynman diagrams in Fig. 1. The calculations are carried out in two steps by following the same procedure as in Ref. [23], where further details can be found. First, a configuration space is selected that

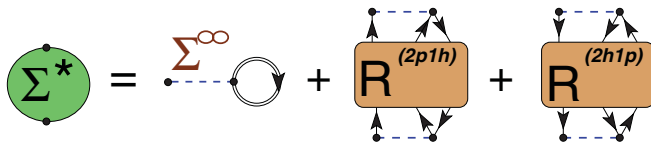


FIG. 1. (Color online) Self-energy $\Sigma^*(E)$ separates exactly into a static (mean-field) term Σ^∞ and the polarization propagators $R^{(2p1h/2h1p)}(E)$ for the 2p1h/2h1p motion. These $R(E)$ are expanded in terms of particle-vibration couplings as depicted below in Fig. 3.

should be as large as possible to account for the treatment of a nuclear collective motion. We then account for the short-range part of a realistic NN interaction by directly calculating the two-body scattering for nucleons that propagate outside the model space. The result is the so-called G -matrix that must be employed as an energy-dependent effective interaction inside the chosen space. The contribution from ladder diagrams from outside the model space is also added to the calculated self-energy and results in an energy-dependent correction to Σ_{ab}^∞ [see Eq. (4)]. When the corresponding self-energy is calculated, this energy dependence enhances the reduction of the spectroscopic strength of occupied orbits by about 10%. A similar depletion is also obtained in nuclear-matter calculations with realistic interactions [17] and confirmed by high-energy electron scattering data [29,30]. The details of this partitioning procedure are presented in Ref. [23]. For the present discussion, it should be clear that this corresponds to calculating separately the contribution of propagators that lie outside the model space and then to add it to the final FRPA results. This does not introduce phenomenological parameters, and the calculation should be regarded as a microscopic study based only on the original realistic interaction.

In addition to the influence of short-range (and tensor) correlations, it is essential to consider the role of long-range correlations in which nucleons couple to low-lying collective states and giant resonances. This is calculated in the second step inside the model space by employing the FRPA method. The physics content of the FRPA is better summarized by looking at its diagrammatic expansion illustrated in Figs. 2 and 3. The basic ingredients are the particle-hole (ph) polarization propagator $\Pi_{\alpha\beta,\gamma\delta}(E)$, that describes excited states of the A -nucleon system, and the two-particle propagator $g_{\alpha\beta,\gamma\delta}^{II}(E)$, that describes the propagation of two added/removed particles. These propagators are calculated as summations of ring and ladder diagrams in the random-phase approximation (RPA). This allows for a proper description of collective excitations in the giant-resonance region when the model space is sufficiently large. The RPA induces time orderings as those shown in Fig. 2 for the ph case and accounts for the presence of two-particle–two-hole and more complicated admixtures in the ground state, which are generated by correlations. In the FRPA, the $R^{(2p1h)}(E)$ and $R^{(2h1p)}(E)$ propagators that appear

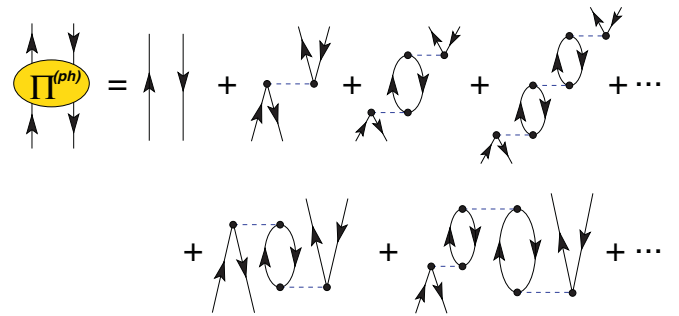


FIG. 2. (Color online) Expansion of the ph propagator $\Pi(E)$ in a series of ring diagrams. The second line gives examples of time-inversion patterns that are generated by the RPA. A similar expansion, in terms of ladders diagrams, applies to $g^{II}(E)$. The diagrams are time ordered, with time propagating upward.

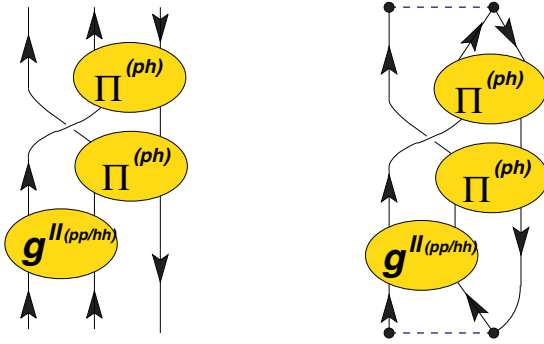


FIG. 3. (Color online) Left: Example of one of the diagrams for $R^{(2p1h)}(E)$ that are summed to all orders by means of the Faddeev method. Each of the ellipses represent an infinite sum of rings $[\Pi(E)]$ or ladders $[g^{II}(E)]$. The diagrams included in $\Pi(E)$ are shown in Fig. 2, and $g^{II}(E)$ is the analogous one for ladders [18]. Right: Corresponding contribution to the self-energy obtained from $R^{(2p1h)}(E)$ (compare to Fig. 1).

in Fig. 1 are obtained by recoupling $\Pi(E)$ and $g^{II}(E)$ to single-particle or hole states, as shown in Fig. 3. This is done by solving the set of Faddeev equations detailed in Refs. [18,19]. Contributions from ph, particle-particle, and hole-hole excitations in all possible partial waves are included in the FRPA as this is required for a complete solution of the problem. Moreover, $R^{(2p1h)}(E)$ and $R^{(2h1p)}(E)$ also include energy-independent vertex corrections to ensure consistency with perturbation theory up to third order to guarantee accurate results at the Fermi surface [31]. We refer the reader to Ref. [18] for more details.

Green's function theory—and in particular the FRPA— involves infinite summations of linked diagrams. This implies that computational requirements scale favorably with the increase of the model-space size and that the method is size extensive, which allows controlling theoretical errors when increasing the size of the system. The FRPA method has been tested in purely *ab-initio* calculations of ${}^4\text{He}$ in Ref. [20] and was found to achieve accuracies comparable to coupled-cluster results [32]. The further advantage of the FRPA formalism is that it calculates explicitly the effects of *all* many-body excitations including the region of giant resonances. The result is a global description of the self-energy over a wide range of energies. The FRPA is then the method of choice for our purpose of investigating medium-mass nuclei in a wide energy domain around the Fermi surface.

III. CALCULATIONS

Extremely large model spaces are not required for the present analysis because we already account for the short-range part of the interactions through the partitioning procedure described in Sec. II C [23]. In the energy regime we are interested in, short-range physics affects mainly the real part of the self-energy in the domain of interest. The contributions to the imaginary part are not included as they show up at very high positive energies which are not considered here [17]. The self-energies of ${}^{40}\text{Ca}$, ${}^{48}\text{Ca}$, and ${}^{60}\text{Ca}$ were calculated using the FRPA in a harmonic-oscillator model space with frequency

$\hbar\Omega = 10$ MeV. Calculations for ${}^{60}\text{Ca}$ were possible in no-core model spaces including up to eight major shells ($N_{\text{max}} = 7$), and we therefore employed this truncation for all the results presented in Sec. IV. This space is deemed large enough to provide a proper description of the physics around the Fermi surface and qualitatively good at energies in the region of giant-resonance excitations which are of interest in this study.

In this work we will mostly focus on averaged properties of the self-energy, as described by the volume integrals (11), for which meaningful results can be obtained. Due to the unavoidable truncation of the model space, calculations will be reliable within an energy interval centered around E_F . We checked these limits by calculating J_W of ${}^{48}\text{Ca}$ for model spaces of different sizes, including up to 10 major oscillator shells (which is possible for this isotope [24]). As expected, results are similar over a range of energies that increases with N_{max} . Based on this comparison, we deduce that the self-energies calculated for $N_{\text{max}} = 7$ (eight shells) and discussed in this work will be meaningful for energies in the range $-80 \text{ MeV} < E - E_F < 80 \text{ MeV}$.

We report results obtained using the realistic Argonne AV18 potential [33] which is local and contains a strongly repulsive core. Calculations based on the softer and nonlocal N3LO interaction [34] gave only slightly less absorption for $E > E_F$, especially in ${}^{40}\text{Ca}$. Nevertheless, the results for the two interactions are qualitatively similar, and we limit the discussion to the AV18 case.

IV. RESULTS

A. Angular-momentum dependence

Figure 4 gives an overall example of the features of the real part of the self-energy, J_V^ℓ . These results are shown for neutrons in ${}^{40}\text{Ca}$, employing the AV18 interaction, and are separated in partial waves up to $\ell = 5$. The variation of J_V^ℓ with respect to

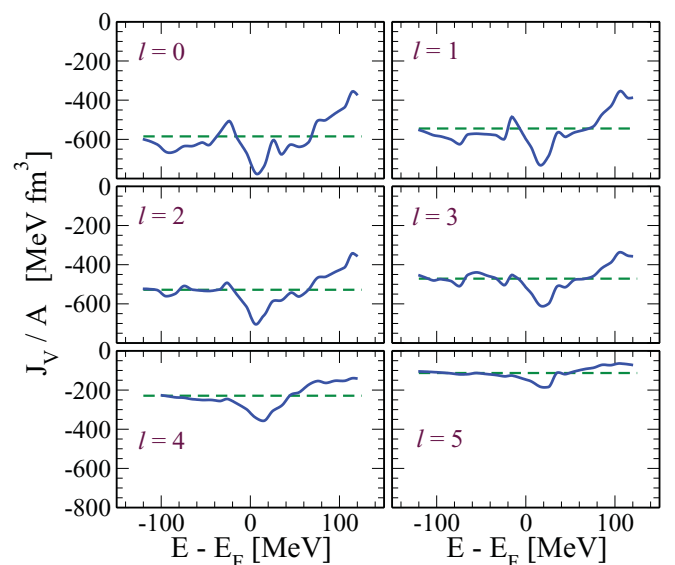


FIG. 4. (Color online) Volume integrals of $\text{Re } \Sigma_0^\ell$ for neutrons in ${}^{40}\text{Ca}$. The horizontal, dashed lines are the volume integrals of $\Sigma_0^{\infty, \ell}(E_F)$.

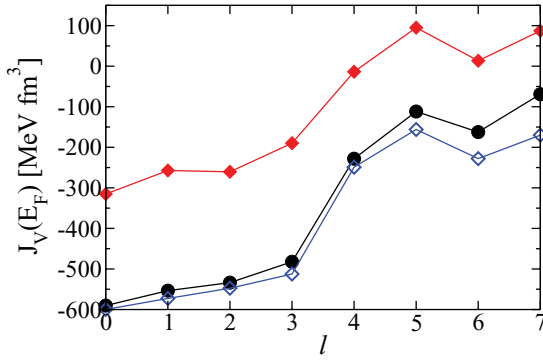


FIG. 5. (Color online) Angular momentum dependence for the volume integrals $J_F^\ell = J_V^\ell(E_F)$ of $\Sigma_0^{\infty,\ell}(E_F)$ excluding the contribution of the dynamic part of the self-energy. For each ℓ , results for protons are given by solid diamonds and neutrons by solid circles. Proton potentials are considerably less attractive due to the Coulomb energy. When the Coulomb interaction is suppressed (open diamonds), the proton results are close to the neutron results. The results shown are for ^{40}Ca using the AV18 interaction.

$J_F^\ell = J_V^\ell(E_F)$ obtained from $\Sigma_0^{\infty,\ell}(E_F)$ also decreases with increasing ℓ (Fig. 4). This reflects a similar reduction of the imaginary parts J_W^ℓ , to which J_V^ℓ are linked through the dispersion relation. The effect may be partly explained by the truncated model space, since the higher ℓ channels also have fewer active orbits. On the other hand, the horizontal lines in Fig. 4, which are the contributions of $\Sigma_0^{\infty,\ell}$ to $J_F^\ell = J_V^\ell(E_F)$, clearly suggest that most of this decrease must arise from the ℓ dependence implied by the nonlocality of the potential. Such an ℓ dependence suggests that it may be important to include nonlocal features in DOM potentials. In Fig. 5 the volume integrals $J_F^\ell = J_V^\ell(E_F)$ are shown excluding the contribution of the dynamic part. Note that because the proton potential is not as deep as that of the neutrons, the volume integral will be smaller for protons than for neutrons. When the calculation is done without the Coulomb potential, the volume integrals for the protons are comparable to those for the neutrons.

This effect of nonlocality can be illustrated by taking, e.g., the energy dependence of the volume contribution of a DOM potential [9] and replacing the radial form factor by a nonlocal potential. The radial parameters of such a nonlocal potential employed here correspond to the nonlocal Hartree-Fock potential of Ref. [35]. Such a nonlocal potential is of the form proposed by Perey and Buck [36] and contains a Gaussian form factor describing the nonlocality. The results are shown in Fig. 6. Since the nonlocal potential depends on the angle between \mathbf{r} and \mathbf{r}' there is an automatic ℓ dependence of the projected J_W^ℓ that exhibit a systematic decrease in absorption for increasing ℓ . While it is apparently possible to fit elastic scattering data with local potentials, a nonlocal potential has a substantial effect on the interior scattering wave function and therefore, e.g., on the analysis of transfer reactions that rely on such wave functions [37,38].

The possible importance of nonlocality for the calculation of observables below the Fermi energy was pointed out in Ref. [35]. When the real part of the self-energy at the Fermi energy is represented by a truly nonlocal potential, it becomes

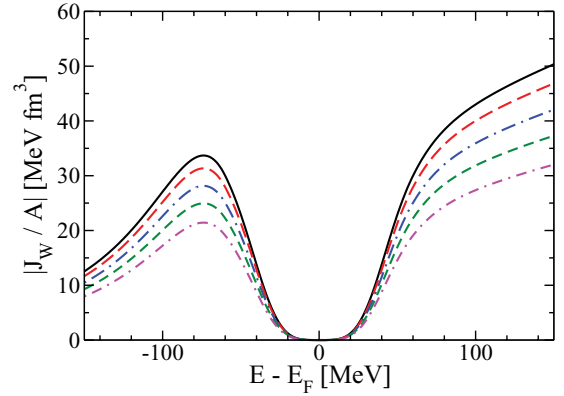


FIG. 6. (Color online) Imaginary volume integrals of the volume part of a DOM self-energy with a local Woods-Saxon form factor replaced by a nonlocal form proposed by Perey and Buck. The results shown are for $\ell = 0$ (solid), $\ell = 1$ (long dash), $\ell = 2$ (long dot dash), $\ell = 3$ (short dash), and $\ell = 4$ (short dot dash).

possible to properly calculate the spectral functions below the Fermi energy and observables like the charge density. The importance of nonlocality for the imaginary part of the self-energy suggested by the FRPA calculations may actually provide a handle on describing the nuclear charge density for ^{40}Ca more accurately than was possible in Ref. [35].

A direct comparison of ℓ -averaged FRPA volume integrals with the corresponding DOM result is made in Fig. 7. Since the DOM results are calculated from a local potential, they must be corrected by the effective mass that governs nonlocality [6,35] before they can be compared with the FRPA results, which are generated from nonlocal potentials. The overall effect of this correction is to enhance the absorption. Referring to Fig. 7, one can see that the FRPA exhibits different behavior above and below E_F than is assumed in the DOM. The

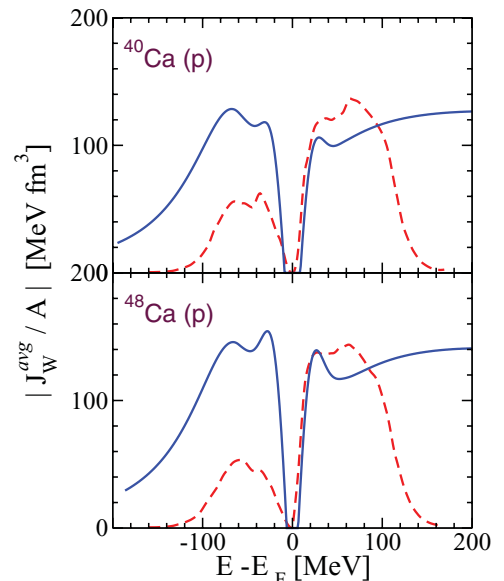


FIG. 7. (Color online) FRPA results for the average over all ℓ channels (dashed) are compared with the DOM result (solid), corrected for nonlocality.

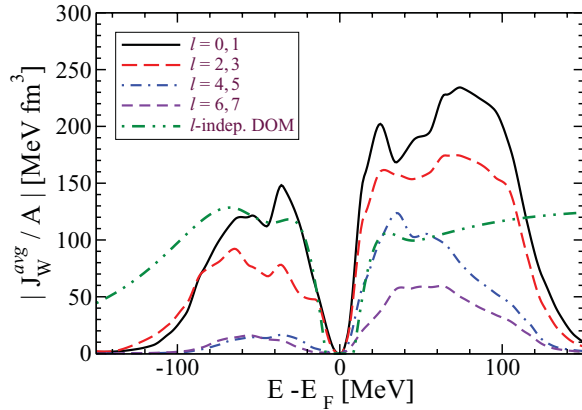


FIG. 8. (Color online) Separate partial wave contributions of J_W averaged over ℓ channels with the same number of harmonic-oscillator orbits in the model space. This plot is for neutrons in ^{40}Ca . The dashed–double-dotted curve represents the DOM result.

FRPA predicts that there is significantly less absorption below E_F than above, whereas according to the assumptions made in a DOM fit, the absorption is roughly symmetric above and below up to about 50 MeV away from E_F [6,8–10]. While this assumption is made in the local version of the DOM, the transition to a nonlocal implementation distorts this assumption of symmetry because the attendant correction involving the effective mass is different above and below the Fermi energy as can be seen in Fig. 7. Since only the absorption above the Fermi energy is strongly constrained by elastic scattering data, it is encouraging that the ℓ -averaged FRPA result is reasonably close to the DOM fit for both nuclei in the domain where the FRPA is expected to be relevant on account of the size of the chosen model space.² The simplifying assumptions of a symmetric absorption around E_F and locality in the DOM generate unrealistic occupation of higher ℓ values below the Fermi energy which is not obtained in the FRPA. More insight into this result is obtained in Fig. 8 where the volume integral is averaged over ℓ channels with the same number of harmonic-oscillator orbits inside the chosen model space for neutrons in ^{40}Ca . Below the Fermi energy the contribution with three (dashed line) and four (solid line) orbits dominate due to the prevalence of low- ℓ orbits like s , p , and d . Higher ℓ values are less relevant below the Fermi energy and this is clearly illustrated in the figure. The dashed–double-dotted curve illustrates the DOM result, which is also shown as the solid curve in the upper panel of Fig. 7 (proton and neutron imaginary potentials are the same in the DOM for ^{40}Ca). The DOM result should therefore probably be compared below the Fermi energy with curves corresponding to the dominant ℓ values, whereas above the Fermi energy the higher ℓ values play a more prominent role. Nevertheless, it is clear that the DOM overestimates the absorption of partial waves below the Fermi energy that

²Note that the calculated J_W decreases quickly at energies $E - E_F > 100$ MeV due to the truncation of the model space. Instead, the DOM predicts correctly that it remains sizable even at higher energies.

TABLE I. Particle-hole gaps in MeV.

		AV18	N3LO	DOM	Expt.
^{40}Ca	ν	10.7	12.0	7.79	7.23
	π	7.9	12.1	7.20	7.24
^{48}Ca	ν	4.8	4.9	2.83	4.79
	π	11.6	13.5	6.78	6.18
^{60}Ca	ν	4.9	6.5	4.95	
	π	10.4	12.3	6.13	

are Pauli blocked in agreement with the observations in Ref. [35].

Further comparison of the FRPA with the DOM self-energy is made in Table I for the ph gap. The AV18 seems to provide smaller ph gaps by 1–2 MeV compared to N3LO. However, in both cases these gaps substantially overestimate the experimental results (see Table I). The DOM fits from Ref. [9] are also included in the table and are typically closer to experiment.

B. Parity dependence

In Fig. 9, the absorption of the negative parity channels is compared with that of the positive parity channels in ^{40}Ca , ^{48}Ca , and ^{60}Ca . The averages $(\sum_{\text{even } \ell} J_W^\ell)/N_{\text{even } \ell}$ and $(\sum_{\text{odd } \ell} J_W^\ell)/N_{\text{odd } \ell}$ are shown to see the trends more clearly. An interesting feature in ^{40}Ca is that just below E_F there is more negative parity absorption than for even parity, while just above E_F the opposite is true. The effect can be understood in terms of the number of 2p1h and 2h1p states, which are the configurations beyond the mean-field approximation that are closest to E_F . In these states, the ph and the hole-particle (hp) phonons have negative parity, since the holes are in the sd shell while the particles are in the pf shell. Thus, near E_F ,

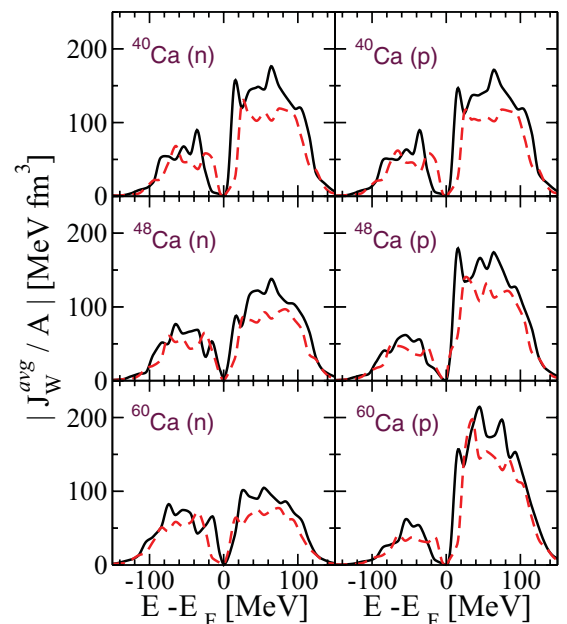


FIG. 9. (Color online) J_W averaged over even ℓ channels (solid) is compared with J_W averaged over odd ℓ channels (dashed).

the 2h1p states will have negative parity and the 2p1h states will have positive parity.

Proton ph configurations at low energy continue to have negative parity as the neutron number increases in the pf shell. However, phonons with positive parity can be created at energies close to E_F due to the partial filling of the neutron pf shell. So, both parities for 2p1h and 2h1p states are possible. As a result, in ^{48}Ca one sees little difference between the absorption from negative and positive parity states.

In ^{60}Ca , which is the next closed shell, the neutron pf shell is filled and the corresponding low-lying neutron ph configurations again have negative parity, as in ^{40}Ca ; but in this case the neutron holes have negative parity corresponding to $\ell = 1$ and 3. Thus, there are more 2h1p states with positive parity near E_F for the neutrons. The situation for the protons is similar to the case of ^{40}Ca . The inversion of the dominant parity above and below E_F is quite general when major shells are filled or depleted and also is visible in the partial waves separately.

C. Asymmetry dependence

The behavior of the nuclear self-energy with changing proton-neutron asymmetry [$\alpha = (N - Z)/A$] has important implications for unstable isotopes. Its understanding is fundamental in obtaining proper *global* parametrizations of the DOM so that these can be trusted in extrapolations toward the drip lines. Moreover, a strong absorption in the optical potential, even if at intermediate energies, affects the absolute quenching of spectroscopic factors [24]. Thus, the study of J_W can in principle contribute to the much-debated asymmetry dependence of spectroscopic factors observed in knockout and transfer reactions [20,37,39–43].

The J_W^{avg} for the three different Ca isotopes are shown in the top panels of Fig. 10. These results predict an opposite behavior of protons and neutrons above E_F , with the proton (neutron) potential increasing (decreasing) when more neutrons are added, qualitatively in agreement with expectations from the Lane potential model [44]. A recent DOM analysis based on several isotopes, including the Ca and Sn chains, employs a similar trend for the volume integrals [10]. However, the same analysis suggests different behavior of the imaginary surface contributions: neutron surface absorption appears to be rather independent of asymmetry, while variations are much stronger for protons and for chains of isotopes tend to increase with asymmetry. The separation between volume and surface effects is an artifact of the functional form chosen for the optical model, and such a separation cannot be carried out uniquely in a fully microscopic approach like the present FRPA. In general, one can argue that most of the physics at scattering energies below 50 MeV is dominated by surface effects which are well covered by the FRPA, whereas volume effects pertain to higher energies, less well covered by the FRPA chosen model space. At energies below the Fermi surface, the overall absorption of both protons and neutrons does not show much variation with changing asymmetry. Since the DOM analysis employs less data from energies below E_F , this result must be further tested in future work.

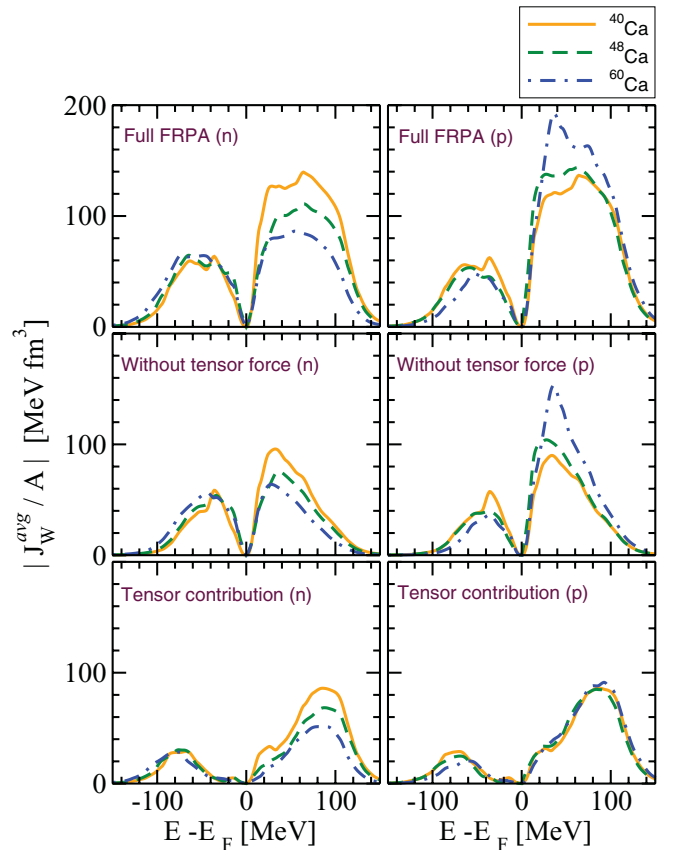


FIG. 10. (Color online) Asymmetry dependence of the absorption for neutrons and protons and dependence on tensor correlations. The top panels show J_W^{avg} for ^{40}Ca (solid) as compared with the results for ^{48}Ca (dashed) and ^{60}Ca (dotted-dashed). The middle panels are obtained by suppressing the tensor component in the AV18 interaction. The difference between the top two panels is plotted in the bottom panels to provide a more detailed assessment of the correlations induced by including the tensor force.

Current DOM implementations assume that surface absorption is similar above and below the Fermi energy, which is clearly not suggested by the FRPA results.

The above pattern, in which one type of nucleon becomes more correlated when increasing the number of its isotopic partners, is a rather general feature in nuclear systems that is also found for asymmetric nucleonic matter [45,46]. FRPA calculations of stable and drip-line nuclei show that this effect results in an asymmetry dependence of spectroscopic factors similar to that observed in knockout reactions, although the overall change from drip line to drip line is rather modest [20]. We note, however, that there also exist other mechanisms that can affect this quenching besides the coupling to the giant-resonance region, including a strong correlation to the ph gap [23] and effects of the continuum at the drip lines [43].

From the characteristics of the above asymmetry dependence, one expects that the nuclear interaction between protons and neutrons plays a major role. The tensor force of the nuclear interaction can provide one such mechanism since it is particularly strong in the $T = 0$ sector. Moreover, it has already been shown to influence the evolution of single-particle

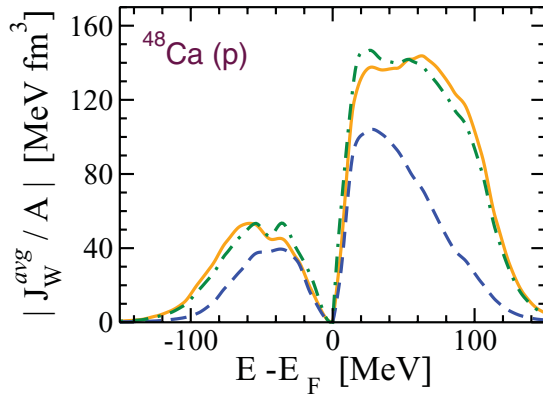


FIG. 11. (Color online) Effect of the tensor force and charge exchange on correlations on the proton- ^{48}Ca self-energy. The solid curve is the imaginary volume integral J_W^{avg} from the full FRPA calculation, while the dashed curve results from removing the tensor term in the AV18 interaction. The dashed-dotted curve is obtained by excluding charge exchange from the full calculation. Similar results are found for neutrons and the other Ca isotopes.

energies at the Fermi surface [47]. To investigate its implication for single-particle properties at energies farther removed from E_F , we recalculated J_W^{avg} by suppressing the tensor component of the AV18 interaction. This is shown in Fig. 11 for protons on ^{48}Ca and in the middle panels of Fig. 10 for all isotopes. Its removal results in a drastic reduction of absorption at energies $|E - E_F| > 30$ MeV. Thus, tensor effects give an important contribution to scattering at these energies. The difference with the complete solution is plotted in the bottom panels of Fig. 10 to highlight the separate effect of the tensor force although this subtraction disregards the presence of interference terms. It is apparent that the tensor force has a very significant effect on the correlations far from the Fermi surface, but it contributes only to the asymmetry dependence of neutron scattering. On the other hand, both scattering and negative energy states near the Fermi surface are dominated by correlations other than tensor which thus produce most of the asymmetry dependence obtained in the full calculation.

In Fig. 11 (dotted-dashed line), we have also calculated the FRPA self-energy by suppressing charge-exchange excitations in the polarization propagator $\Pi(E)$. These contributions correspond to a mechanism in which the proton (neutron) projectile is Pauli exchanged with a neutron (proton) in the target. It was argued that this could enhance surface absorption due to the presence of Gamow-Teller resonances, with strength increasing as $\approx 3(N - Z)$ [9]. However, the FRPA results suggest that charge-exchange excitations of the target interfere only very weakly with the nucleon-nucleus scattering process.

D. Analysis of radial dependence

Improving the analysis of elastic scattering data above the Fermi energy and observables related to quantities below the Fermi energy in a DOM framework appears to depend sensitively on the treatment of nonlocality in the imaginary part of the self-energy [35]. It is therefore useful to gain some insight into the properties of the microscopic FRPA self-energy

in order to provide some guidance for future implementations of nonlocality in the DOM. We therefore performed a few simple fits to represent the central part of the imaginary part of the FRPA self-energy in coordinate space at a given energy assuming the following form of the potential

$$W_{NL}(\mathbf{r}, \mathbf{r}') = W_0 \sqrt{f(r)} \sqrt{f(r')} H\left(\frac{\mathbf{r} - \mathbf{r}'}{\beta}\right). \quad (16)$$

We deviate from the standard Perey prescription for nonlocality by employing square-root factors of the function $f(r)$ which is still represented by the conventional Woods-Saxon form factor

$$f(r) = \frac{1}{1 + e^{\frac{r-R}{a}}}, \quad (17)$$

with $R = r_0 A^{1/3}$. The function H determines the degree of nonlocality and is assumed to be a Gaussian following Ref. [36]:

$$H\left(\frac{\mathbf{r} - \mathbf{r}'}{\beta}\right) = \frac{1}{\pi^{3/2} \beta^3} \exp\left(-\frac{|\mathbf{r} - \mathbf{r}'|^2}{\beta^2}\right). \quad (18)$$

When the angular dependence in H is projected out, an analytic solution is obtained for each orbital angular momentum ℓ :

$$W_{NL}^\ell(r, r') = W_0 \sqrt{f(r)} \sqrt{f(r')} \frac{4}{\pi^{1/2} \beta^3} \times \exp\left(-\frac{-r^2 + r'^2}{\beta^2}\right) i^\ell (-1)^\ell j_\ell(iz), \quad (19)$$

where $z = 2rr'/\beta^2$ and j_ℓ is a spherical Bessel function with a purely imaginary argument. The fact that an analytic projection is possible provided the motivation of the choice of Eq. (16). In arriving at the result of Eq. (19), use has been made of the relation between the spherical Bessel functions and the Legendre polynomials P_ℓ :

$$j_\ell(z) = \frac{1}{2i^\ell} \int_{-1}^{+1} dt e^{izt} P_\ell(t). \quad (20)$$

We have chosen to fit the imaginary part of the FRPA self-energy at an energy of $E - E_F = 44$ MeV, where surface physics dominates. In practice, we consider only a fit to the $\ell = 0$ self-energy since it represents the partial wave with the best convergence properties associated with the limited model space considered. An attempt was made to fit the volume integral of the microscopic self-energy.

In Fig. 12 we display the diagonal of the central imaginary part of the self-energy in coordinate space for $\ell = 0$ for the FRPA self-energy for ^{40}Ca , ^{48}Ca , and ^{60}Ca by solid lines offset by 5 MeV for the different isotopes. The corresponding $\ell = 0$ projections of Eq. (16) given by Eq. (19) are shown by the dashed curves. The fit according to Eq. (16) appears to be quite satisfactory suggesting that a reasonable representation of the microscopic self-energy is possible and may provide a useful starting point for future choices for DOM functionals.

The main characteristic of an absorptive potential is the volume integral. For local potentials this quantity is well constrained by experimental cross sections [9,10]. The properties of the imaginary part of the FRPA self-energy in terms of its nonlocality content are summarized in Table II

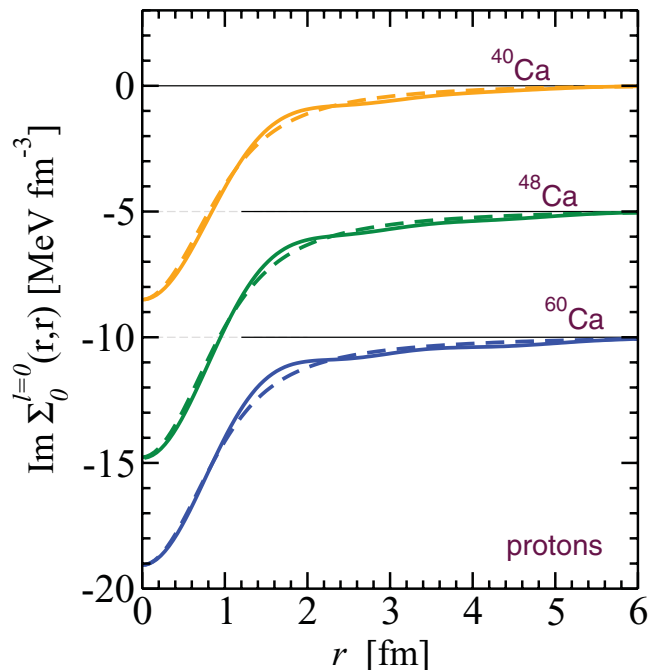


FIG. 12. (Color online) Diagonal part of FRPA imaginary self-energy for protons at $E - E_F = 44$ MeV (solid) and the corresponding parametrized self-energy (dashed). The results shown are for $\ell = 0$ and are offset by 5 MeV for each subsequent nucleus.

for the three different nuclei. The parameters are fitted to reproduce the essential properties of the self-energy including the volume integral for $\ell = 0$. We observe that the values for the diffuseness are larger than standard ones and increase with neutron number. The radius parameter exhibits a similar nonstandard trend. The value of the nonlocality parameter β is also substantially larger than typically assumed for real nonlocal potentials. The DOM analysis of Ref. [35] introduced a nonlocal Hartree-Fock potential to allow the calculation of additional properties below the Fermi energy from the spectral functions that are the solutions of the Dyson equation. The adjusted nonlocality parameter in that work corresponded to 0.91 fm.

The DOM fit to Ca isotopes suggests that surface terms of the neutron imaginary potential should remain more or less unchanged as the neutron drip line is approached [9]. In order to investigate this trend for the microscopic potential we integrate the nonlocal FRPA self-energy over one radial

TABLE II. Parameters from nonlocal fits to the imaginary part of the proton self-energy at $E - E_F = 44$ MeV for ^{40}Ca , ^{48}Ca , and ^{60}Ca . W_0 is in MeV; r_0 , a_0 , β are in fm; and J_W is in units of MeV fm³.

Isotope	W_0	r_0	a_0	β	$ J_W/A $	$ J_W/A $ FRPA
^{40}Ca	14.1	1.23	1.23	1.54	187	188
^{48}Ca	16.1	1.32	1.30	1.54	242	241
^{60}Ca	13.6	1.50	1.50	1.49	266	268

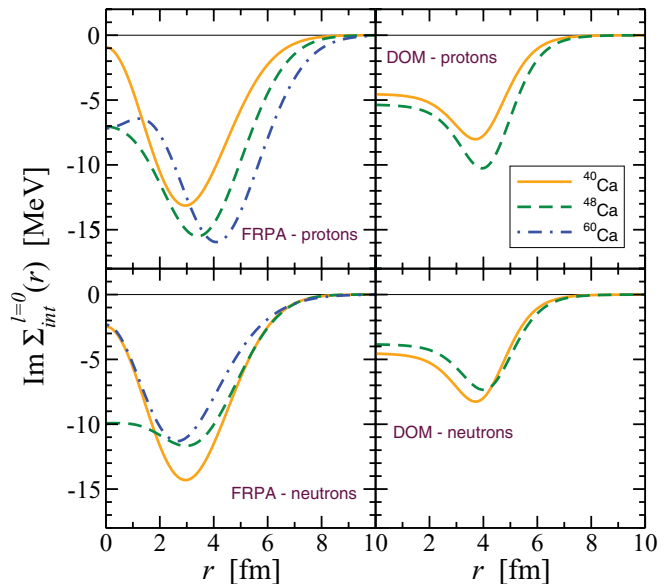


FIG. 13. (Color online) Left panels: FRPA imaginary self-energy integrated over r' for protons in ^{40}Ca (solid), ^{48}Ca (dashed), and ^{60}Ca (dotted-dashed), see Eq. (21). The results shown are for $\ell = 0$ and at an energy of 44 MeV above E_F . Right panels: For comparison, the DOM imaginary potentials at the same energy are shown for ^{40}Ca and ^{48}Ca . Since these are local, they have been corrected for nonlocality by the k mass.

coordinate,

$$\Sigma_{\text{int}}^{\ell}(r; E) = \int dr' r'^2 \Sigma_0^{\ell}(r, r'; E), \quad (21)$$

for the partial wave $\ell = 0$. This is compared to the DOM fit in Fig. 13 at the same energy $E - E_F = 44$ MeV. In accordance with the DOM analysis, we find that the contribution to the proton imaginary part in the surface region increases with the neutron number. The neutron potential changes very little at the surface between ^{40}Ca and ^{48}Ca , also in agreement with the DOM assumption. However, FRPA neutron absorption at the surface decreases more substantially when going all the way to ^{60}Ca , pointing out that a simple extrapolation of the surface term to very large asymmetries may not be trivial.

V. CONCLUSIONS

In this investigation, an attempt was made to establish links between the DOM—an empirical approach to the nuclear-many-body problem based on the framework of the Green's function method and relevant experimental data—and the microscopic FRPA approach. An analysis of the volume integrals calculated from both approaches proved to be a useful link, and on the whole, both the DOM and the FRPA produced similar results. However, there were some significant and illuminating differences.

The FRPA exhibits some important shell effects as neutrons are added to ^{40}Ca . In particular, there is a parity dependence in ^{40}Ca and ^{60}Ca , but not in ^{48}Ca , where both parities occur at low energy due to the partial filling of the neutron pf shell. Such an effect has not hitherto been taken into account in the

DOM. Inspection of the imaginary volume integrals generated by the FRPA also calls into question the assumption in most DOM analyses that the imaginary part is symmetric about E_F for the surface absorption, suggesting that absorption of high- ℓ waves corresponding to unoccupied orbits is suppressed below E_F . Further insight into the underlying physics of DOM potentials is provided by the observation that a substantial contribution to the absorption is due to the NN tensor force. This influence becomes dominant at energies about 40 MeV above or below E_F . For protons, however, most of the observed asymmetry dependence of the absorption at positive energy in the DOM fits appears to be due to central components of the interaction. For neutrons the decrease in absorption at positive energy obtained with the FRPA must be contrasted with the weaker effects deduced so far from DOM fits. Noteworthy is also the relevance of the nonlocality of the absorption process obtained from the microscopic FRPA. It leads to an important ℓ dependence that may play an important role in explaining

data like the nuclear charge density that are associated with properties of the self-energy below the Fermi energy. Its role in scattering processes remains to be studied as well and has important consequences for the analysis of transfer and knockout reactions which are sensitive to interior wave functions generated by optical potentials.

ACKNOWLEDGMENTS

This work was supported by the US National Science Foundation under Grant Nos. PHY-0652900 and PHY-0968941, by the Japanese Ministry of Education, Science, and Technology (MEXT) under KAKENHI Grant No. 21740213, and by the United Kingdom Science and Technology Facilities Council (STFC) through Travel Grant No. ST/I003363. S.J.W. acknowledges support from JUSTIPEN (Japan-US Theory Institute for Physics with Exotic Nuclei) under grant number DEFG02-06ER41407 (U. Tennessee).

-
- [1] F. D. Becchetti Jr. and G. W. Greenlees, *Phys. Rev.* **182**, 1190 (1969).
- [2] R. L. Varner, W. J. Thompson, T. L. McAbee, E. J. Ludwig, and T. B. Clegg, *Phys. Rep.* **201**, 57 (1991).
- [3] A. J. Koning and J. P. Delaroche, *Nucl. Phys. A* **713**, 231 (2003).
- [4] C. Mahaux, P. F. Bortignon, R. A. Broglia, and C. H. Dasso, *Phys. Rep.* **120**, 1 (1985).
- [5] C. Mahaux and R. Sartor, *Phys. Rev. Lett.* **57**, 3015 (1986).
- [6] C. Mahaux and R. Sartor, *Adv. Nucl. Phys.* **20**, 1 (1991).
- [7] W. H. Dickhoff and D. Van Neck, *Many-Body Theory Exposed!*, 2nd. ed. (World Scientific, New Jersey, 2008).
- [8] R. J. Charity, L. G. Sobotka, and W. H. Dickhoff, *Phys. Rev. Lett.* **97**, 162503 (2006).
- [9] R. J. Charity, J. M. Mueller, L. G. Sobotka, and W. H. Dickhoff, *Phys. Rev. C* **76**, 044314 (2007).
- [10] J. M. Mueller *et al.*, *Phys. Rev. C* **83**, 064605 (2011).
- [11] H. Feshbach, *Ann. Phys.* **5**, 357 (1958).
- [12] H. Feshbach, *Ann. Phys.* **19**, 287 (1962).
- [13] F. Capuzzi and C. Mahaux, *Ann. Phys.* **245**, 147 (1996).
- [14] K. Amos, P. J. Dortmans, H. V. von Geramb, S. Karataglidis, and J. Raynal, *Adv. Nucl. Phys.* **25**, 275 (2000).
- [15] J. S. Bell and E. J. Squires, *Phys. Rev. Lett.* **3**, 96 (1959).
- [16] J. Escher and B. K. Jennings, *Phys. Rev. C* **66**, 034313 (2002).
- [17] W. H. Dickhoff and C. Barbieri, *Prog. Part. Nucl. Phys.* **52**, 377 (2004).
- [18] C. Barbieri, D. Van Neck, and W. H. Dickhoff, *Phys. Rev. A* **76**, 052503 (2007).
- [19] C. Barbieri and W. H. Dickhoff, *Phys. Rev. C* **63**, 034313 (2001).
- [20] C. Barbieri, in *Proceedings of the 12th International Conference on Nuclear Reaction Mechanisms*, edited by F. Cerutti and A. Ferrari (CERN, Geneva, 2010), Vol. 1, p. 137; [arXiv:0909.0336v2](https://arxiv.org/abs/0909.0336v2).
- [21] C. Barbieri and W. H. Dickhoff, *Phys. Rev. C* **65**, 064313 (2002).
- [22] M. Degroote, D. Van Neck, and C. Barbieri, *Phys. Rev. A* **83**, 042517 (2011).
- [23] C. Barbieri and M. Hjorth-Jensen, *Phys. Rev. C* **79**, 064313 (2009).
- [24] C. Barbieri, *Phys. Rev. Lett.* **103**, 202502 (2009).
- [25] G. J. Kramer, H. P. Blok, and L. Lapikás, *Nucl. Phys. A* **679**, 267 (2001).
- [26] C. Barbieri and B. K. Jennings, *Phys. Rev. C* **72**, 014613 (2005).
- [27] G. E. Brown and M. Rho, *Nucl. Phys. A* **372**, 397 (1981).
- [28] G. W. Greenlees, G. J. Pyle, and Y. C. Tang, *Phys. Rev.* **171**, 1115 (1968).
- [29] D. Rohe *et al.*, *Phys. Rev. Lett.* **93**, 182501 (2004).
- [30] C. Barbieri and L. Lapikás, *Phys. Rev. C* **70**, 054612 (2004).
- [31] A. B. Trofimov and J. Schirmer, *J. Chem. Phys.* **123**, 144115 (2005).
- [32] G. Hagen, D. J. Dean, M. Hjorth-Jensen, T. Papenbrock, and A. Schwenk, *Phys. Rev. C* **76**, 044305 (2007).
- [33] R. B. Wiringa, V. G. J. Stoks, and R. Schiavilla, *Phys. Rev. C* **51**, 38 (1995).
- [34] D. R. Entem and R. Machleidt, *Phys. Rev. C* **68**, 041001 (2003).
- [35] W. H. Dickhoff, D. Van Neck, S. J. Waldecker, R. J. Charity, and L. G. Sobotka, *Phys. Rev. C* **82**, 054306 (2010).
- [36] F. Perey and B. Buck, *Nucl. Phys.* **32**, 353 (1962).
- [37] F. M. Nunes, A. Deltuva, and J. Hong, *Phys. Rev. C* **83**, 034610 (2011).
- [38] R. C. Johnson, *Phys. Rev. C* **80**, 044616 (2009).
- [39] A. Gade *et al.*, *Phys. Rev. C* **77**, 044306 (2008).
- [40] J. Lee *et al.*, *Phys. Rev. Lett.* **104**, 112701 (2010).
- [41] N. K. Timofeyuk, *Phys. Rev. Lett.* **103**, 242501 (2009).
- [42] J. Lee *et al.*, *Phys. Rev. C* **83**, 014606 (2011).
- [43] Ø. Jensen, G. Hagen, M. Hjorth-Jensen, B. A. Brown, and A. Gade, *Phys. Rev. Lett.* **107**, 032501 (2011).
- [44] A. M. Lane, *Nucl. Phys.* **35**, 676 (1962).
- [45] T. Frick, H. Mütter, A. Rios, A. Polls, and A. Ramos, *Phys. Rev. C* **71**, 014313 (2005).
- [46] A. Rios, A. Polls, and W. H. Dickhoff, *Phys. Rev. C* **79**, 064308 (2009).
- [47] T. Otsuka, T. Suzuki, R. Fujimoto, H. Grawe, and Y. Akaishi, *Phys. Rev. Lett.* **95**, 232502 (2005).